Unintended Phosphorus Doping of Nickel Nanoparticles during Synthesis with TOP: A Discovery through Structural Analysis

Liane M. Moreau,[†] Don-Hyung Ha,[†] Clive R. Bealing, Haitao Zhang, Richard G. Hennig, and Richard D. Robinson*

Department of Materials Science and Engineering, Cornell University, Ithaca, New York 14853, United States

S *Supporting Information*

ABSTRACT: We report the discovery of unintentional phosphorus (P) doping when tri-*n*-octylphosphine (TOP) ligands are used in Ni nanoparticle synthesis, which is the most common method for monodisperse Ni nanoparticle synthesis. The nanoparticles appear pure face-centered cubic (fcc) Ni in X-ray diffraction despite the surprisingly high level (5 atomic %) of P. We find that the P doping follows a direct relationship with increased reaction time and temperature and that the P doping can be estimated with the degree of lattice expansion shown from a peak shift in the XRD spectrum. Through EXAFS modeling and density-functional (DFT) calculations of defect formation energies we find that the P atoms are preferentially located on the fcc lattice as substitutional dopants with oxidation state of zero. Magnetic and catalytic properties are shown to be greatly affected by this doping; DFT calculations show magnetization losses in the Ni system, as well as in Fe and Co systems. These findings are likely relevant for other metal syntheses that employ phosphine ligands.

KEYWORDS: *EXAFS, doping, nanoparticles, TOP, nickel, phosphorus*
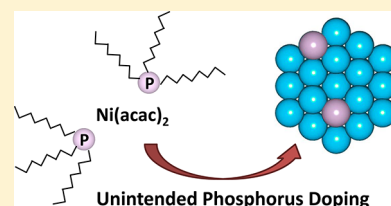
For nearly two decades the backbone of colloidal nanoparticle synthesis has been the organic molecules that serve as both surfactants and solvents for the nanoparticles and precursors.[1−3] The common ligands and solvents used are bulky hydrocarbon molecules, such as oleic acid, tri-*n*-octylphosphine oxide (TOPO), tri-*n*-octylphosphine (TOP), and phosphonic acids. These coordinating molecules play a crucial role in controlling the size and morphology of the nanoparticles, stabilizing the nanoparticles, and solvating the precursors.[2,4,5] These reagents had generally been considered pure and were believed to play only a supporting role in the synthesis. However, recent papers have provided a more complex story,[6] such as elucidating the role of impurities[7,8] and coordination groups,[9] and even identifying the unexpected reactiveness of TOPO being used as a phosphorus source.[10] In this work, we find that a commonly used surfactant in Ni nanoparticle synthesis, TOP, can act as a P source during synthesis, leading to unintended P doping.

Nickel nanostructures are of increasing interest for their novel magnetic and catalytic properties. Nickel nanoparticles have been shown to decrease the activation energy of hydrogen desorption by surface activation, enhancing catalytic activity.[11] They have also demonstrated functionality as catalysts for the decomposition of hydrazine[12] and hydrogenation reactions[13,14] and enhance the hydrogen storage capacity of carbon nanotubes by up to three times.[15−18] In recent years, organic-phase synthesis of Ni nanoparticles using TOP as a surfactant[19−24] has resulted in better control of particle size and morphology. This is an important achievement because catalytic activity has been shown to increase in liquid phase dehydrogenation reactions with smaller particles[25] and

magnetic properties of Ni nanoparticles are highly dependent on particle size.[26] For instance, Carenco et al. performed a specific study of Ni nanoparticle synthesis using TOP as a surfactant.[27] They determined that TOP was crucial to achieve monodisperse Ni nanoparticles in comparison to other methods and report the synthesis of monodisperse Ni nanoparticles with a tunable size range from 2 to 30 nm. On the basis of X-ray diffraction (XRD), all previous studies characterized their Ni nanoparticles as pure face-centered cubic (fcc) Ni.[19,21−24,27]

In our study, we have synthesized Ni nanoparticles following similar procedures involving TOP and have found that the composition is not pure Ni. In particular, we discover that the Ni particles, despite their characterization as pure fcc Ni based on XRD, contain a significant amount of phosphorus. The excess P content has property implications not previously realized, especially with respect to magnetism and catalysis. We determine by density functional calculations that magnetic properties dramatically decrease with increasing P content. Catalytic behavior should also be affected: we find that there are some significant differences in the electronic density of states (DOS) near the Fermi energy with P doping. Equally surprising is the location and charge of the P atoms in the lattice: a majority of P atoms sit substitutionally on the fcc lattice sites and were found through calculations to be charge neutral (P^0).

Although techniques that enable the structural characterization of bulk material have been well-developed, the dominance of surface facets, small size, and poor crystalline order makes characterization of nanoparticles difficult. X-ray absorption spectroscopy (XAS) is a powerful method to study local atomic arrangements and has been used to resolve the structure of colloidal nanocrystals.[28−35] With the use of high energy, white-light synchrotron radiation, sensitive XAS spectra can be obtained and used to gain insight into materials' structural properties.[36,37] Using both the lower-energy X-ray absorption near edge structure (XANES) portion of the spectrum to resolve electronic and geometric structure, and the higher-energy quasi-periodic EXAFS (extended X-ray absorption fine structure) modulations to resolve radial structure, the structure of both XRD-detectable and XRD-amorphous materials can be determined in fine detail.[38]

XAS in combination with other characterization methods, such as XRD, density-functional theory (DFT), inductively coupled plasma (ICP), transmission electron microscopy (TEM), and superconducting quantum interference device (SQUID) measurements, allows for resolution of composition, structure, and property relationships in complex nanomaterials. EXAFS and XRD complement each other by providing insight into short-range and long-range order, respectively. DFT enables calculation of formation energies to determine lowest-energy compositional configurations and charge analysis for dopant atoms.[39,40] TEM provides morphological and size-distribution insight, ICP provides the atomic composition, and SQUID enables the study of magnetic properties. Thus a complete picture of the nanoparticle structural properties can be obtained through cooperative use of these methods.

In this investigation, we (1) report a surprisingly high amount of P present in the fcc Ni nanoparticles that results from routine synthesis and show that the P doping in the fcc Ni nanoparticles increases as a function of reaction time and temperature, (2) present the structural attributes (interatomic distances, distortion, coordination, and composition) of the Ni nanoparticles resulting from the P atom doping, (3) demonstrate the feasibility of significant phosphorus stability within an fcc Ni lattice without significant lattice distortion, (4) reveal the effects of excess P content on the magnetic and catalytic properties, and the stability of both amorphous and crystalline phases that comprise transition metal nanoparticles, (5) compare the long-range structural characterization by XRD with the radial structure information obtained from EXAFS analysis, and (6) propose a method to determine the P content of the nanoparticles based as a function of XRD peak position. Because of the intimate connection between nanoscale structural attributes and their resulting properties, control over nanoparticle structure and doping will enable the tailoring of their properties for magnetic and catalytic applications.

We briefly describe the synthesis conditions for the nanoparticles. Complete descriptions of all characterization and analysis methods can be found in the Supporting Information. Synthesis of the Ni nanoparticle samples was based on thermal decomposition of a Ni-TOP complex as outlined by Muthuswamy et al.[21] Under air-free conditions, 1.17 g (4 mmol) of nickel acetylacetonate ($Ni(acac)_2$) and 4.48 mmol of TOP were mixed into a flask containing 10 mL of octyl ether (solvent) and 4 mL of oleylamine (surfactant). The solution was heated to 230 °C and the particles were allowed to grow for 1 h. After the reaction, the nanoparticle products were isolated by centrifugation with excess ethanol.

Our Ni nanoparticle recipe falls within the range of conditions previously reported for pure-phase Ni.[19,21,23,27] Methods from the literature for the synthesis of Ni nanoparticles using this same synthetic method use $TOP/Ni(acac)_2$ ratios from 0.8 to 3, temperatures ranging from 200 to 240 °C, and oleylamine/$Ni(acac)_2$ ratios from 3 to 10.[19,21,23,27] Thus, our results in which we find surprisingly high P concentrations in the Ni nanoparticles should be applicable to these previous works.

TEM images show that the Ni particles are monodisperse, which is in agreement with previous studies that use TOP as a surfactant (Figure 1a).[27] The Ni nanoparticles (22.2 nm, std. dev. 8.9%) have a quasi-spherical morphology. High-resolution TEM (HRTEM) results of these particles show them to be polycrystalline (Figure 1b) and XRD results show that each of the Ni nanoparticle peaks matches well with the fcc Ni structure (Figure 1c). The slight contrast on the surface of the nanoparticle sample in Figure 1b is likely due to surface oxidation during the oxygen plasma cleaning procedure (see Supporting Information for method). Prior to plasma cleaning, the nanoparticles have no contributions from nickel phosphide or nickel oxide detected by XRD. From the Scherrer equation, the grain size in these Ni particles is about 5.5 nm, indicating that the Ni particles are polycrystalline, each consisting of several grains, which is consistent with our HRTEM images.

The Ni nanoparticle sample and Ni foil XAS spectra (Figure 2a) share similar features especially within the lower energy XANES region, and therefore exhibit similar electronic structure. The K-edge in both samples is 8334 eV, a value associated with the 1s−3d atomic line.[41,42] Although the spectra for the Ni nanoparticles and the Ni foil show similar features throughout the near-edge and EXAFS regime, there is a noticeable reduction in the Ni nanoparticle sample's EXAFS oscillation amplitude. Also, the Ni nanoparticle spectrum features a white line peak and EXAFS oscillations that are broadened compared to the sharp features in the Ni foil spectrum.

The shape and phase of both the *k*-space and *R*-space XAS spectra are very similar for the Ni nanoparticles and Ni foil (Figure 2b,c). Both samples show significant contributions beyond the first coordination shell, observable in the *R*-space spectrum (Figure 2c). This display of long-range order is characteristic of a crystalline structure.[36] The spectral intensity amplitudes of the Ni nanoparticles, however, are considerably reduced compared to bulk. There is a known amplitude reduction associated with nanoscale effects.[43,44] Theory predicts an intensity reduction of about 8% due to nanoscale effects for our 5.5 nm grains.[45] Experimental reports in related material systems have seen intensity reductions as large as 25% in *k*-space and 20% in *R*-space for 6 nm NiO nanocrystals.[43] Our crystal domains at 5.5 nm should show comparable intensity reductions to these works but we find much larger reductions of ~41% in both *k*- and *R*-space.

The amplitude reduction can be explained by P content. In bulk Ni a reduction in *k*- and *R*-space intensity was previously observed when P was introduced into the lattice.[41] With 8 atomic % P, the reduction was about 20%, and at 10 atomic % P the reduction increased to 47%.[41] In both cases, the lattice retained the fcc structure despite this high level of P content. It is likely that the intensity reductions in our nanoparticle system result from a combination of nanoscale effects and P doping (discussed below).
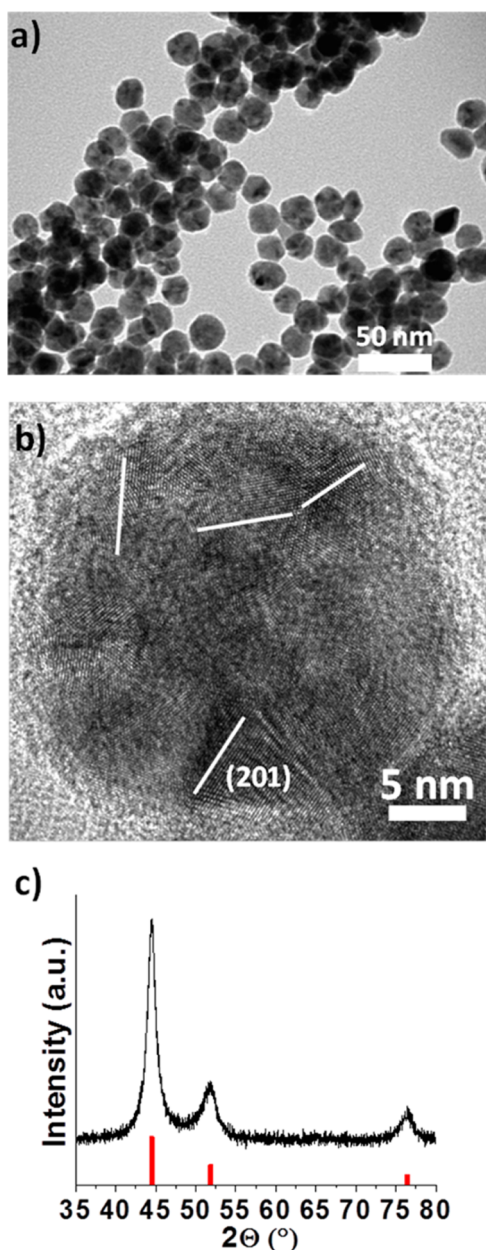
Figure 1. TEM images and XRD spectrum of Ni nanoparticles. (a) TEM images show monodisperse Ni nanoparticles with quasi-spherical morphology. (b) HRTEM image reveals that the Ni nanoparticles are polycrystalline and that they are not core–shell structures. The white lines in the particle present nickel (201) lattice planes indicating multigrains within the nanoparticle. (c) XRD spectrum shows crystalline fcc Ni (red bars correspond to JCPDS 65-2865.).
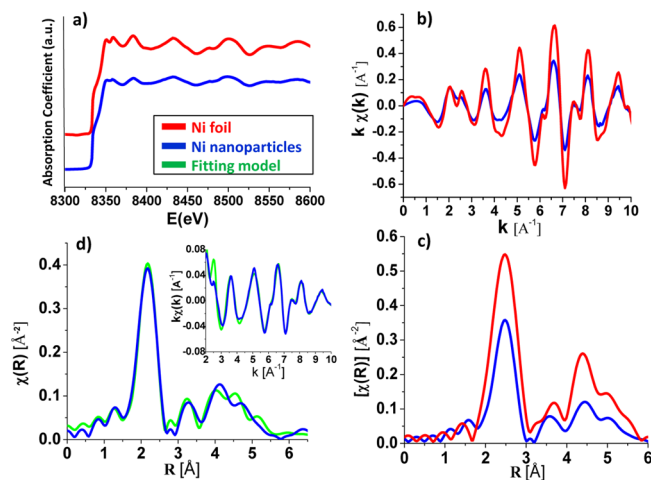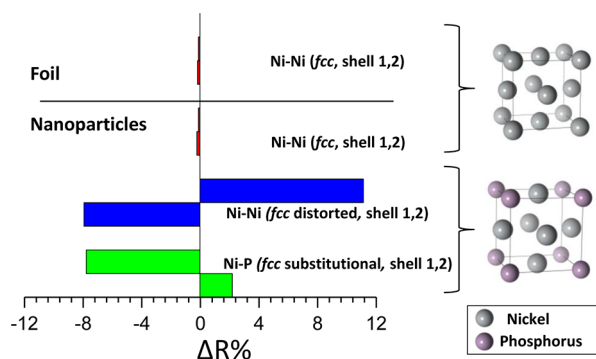

Figure 2. Ni nanoparticles XAS data and EXAFS fitting model. (a) The spectra of the Ni foil (red) and Ni nanoparticles (blue) are shown. Observable broadening is noticeable in the Ni nanoparticle spectrum. (b) Plots of the Ni foil and nanoparticle sample spectra in *k*-space. The shapes of the curves are similar but there is a reduction in amplitude between the Ni foil and Ni nanoparticle sample. (c) Nonphase shifted *R*-space spectra. A high degree of crystallinity is noticeable in the Ni foil and Ni nanoparticle samples, despite significant reduction in the Ni nanoparticle sample peak heights. (d) The theoretical fitting model using fcc Ni and substitutional P is shown in *R*-space and *k*-space (inset). The fitting results (green) are well-matched to the experimental spectra (blue).

Through the EXAFS fitting process we found that it was impossible to resolve the Ni sample with a model that included only a pure, well-ordered fcc Ni crystal structure (see Supporting Information Figure S2a). Degeneracy values reveal that pure fcc Ni alone does not provide an accurate model, despite XRD results, which suggest a pure-phase fcc structure. Using only fcc pathways in the fitting model for the first shell the degeneracy of the model is only 74% that of bulk, meaning that 26% of the Ni–Ni pathway degeneracies are missing (see Supporting Information Table S1). This degeneracy reduction is unphysical for fcc Ni and cannot be ascribed to nanosize effects: using the method proposed by Calvin et al. to estimate

reduction in coordination number due to nanoscale effects, the degeneracy value in our 5.5 nm crystal domains should be 92% of the accepted bulk degeneracy value.[45] Thus the 74% obtained using pure fcc Ni is far too low of a contribution to be accounted for by nanoscale effects, even when the typical 10% error in the coordination numbers determined by the fitting is considered.[29,46,47] Additional structural contributions must therefore exist.

Surface oxidation also does not account for the missing structural contributions. In our previous studies of the Co–P nanoparticle system, additional contributions to the ε-Co structure were attributed to surface oxidation.[48] However, using a combination of Ni fcc and NiO pathways, the fit was also poor (Supporting Information Figure S2b). Much larger degeneracy values were obtained for the second shell than for the first shell for all permutations of the model fit (Supporting Information Table S2), which is unreasonable since the degeneracy values should remain constant or decrease for higher order shells.[43]

A reasonable model was found using a combination of fcc Ni and Ni_2P pathways (see Supporting Information Figure S3, Table S3). Using this combination the fcc pathways became well-ordered, but there was extreme distortion observed in the Ni_2P fitting and atomic positions, particularly for higher shells of Ni_2P. This suggests that the positions of the P atoms do not correspond closely to those in the Ni_2P structure. We examined the radial distances (see Supporting Information Table S4) and realized that a majority (63%) of the Ni–P pathways was within a distance of 3.6% from substitutional fcc positions, and a smaller percentage (17%) corresponded to octahedral interstitial site distances. Using this knowledge we proposed that the P atoms were located primarily on substitutional sites and created a new EXAFS model based on this assumption.

To achieve the best-fit model for the Ni nanoparticle sample we used single and multiple scattering pathways from a combination of fcc Ni and an artificially created fcc lattice built with three Ni atoms and one P atom substituted on the fourth Ni fcc site (e.g., fcc Ni_3P, see Figure 3 and Supporting

Figure 3. Deviation of interatomic distance from reference Ni pathways. Red bars correspond to well-ordered Ni−Ni pathways from the fcc Ni phase, blue bars correspond to Ni−Ni pathways in the Ni_3P fcc model, and green bars correspond to Ni−P pathways in the Ni_3P fcc model. Deviations in interatomic distance between the fitting model and bulk are given for the first two shells, expressed as a percentage of shell distance. Note the large deviations associated with the Ni and P positions in the Ni_3P model. Atomic structures at right show the EXAFS models used for the fitting. At top is the fcc Ni lattice, and on the bottom is the artificial Ni_3P fcc model used to account for P doping and Ni positional distortions, based on fcc Ni with substitutional P atoms.

Information Figure S4). The fcc Ni_3P contributions simulate the P substitution within the Ni fcc lattice and also enable distortion of the Ni atoms surrounding the substitutional P. Thus, the additional degeneracies for the Ni−Ni pathways are accounted for by pathways that are distorted from their Ni fcc positions. These two factors, additional Ni−P pathways and allowing neighboring Ni positions to distort, improved the goodness of the fit to acceptable levels compared to the poor fit from using only a pure-phase fcc Ni model. The substitutional P and particularly the neighboring Ni−Ni pathways deviated from ideal positions with large differences in interatomic distance (exceeding 5% of the average interatomic distance, as shown in Figure 3). The large deviations from ideal positions and the decreased degeneracy of these pathways (see Table 1) indicate that the substitutional P contribution present within

the crystalline fcc Ni lattice distorts the surrounding atoms in the lattice, creating somewhat disordered pathways within the well-ordered fcc structure.

The fcc Ni + substitutional P model has a high quality fit (low R-factor) to the experimental data in both R-space (Figure 2d) and k-space (Figure 2d, inset). Table 1 contains the parameters used to construct the fitting model for the Ni nanoparticles. The parameters included in the table are the reference degeneracy value found in bulk structure (N_{theory})[49] (the number of atoms located at a specified distance from the central scattering atom), the degeneracy value determined by the fit to the experimental spectra (N_{exp}), the reference interatomic distance from the scattering atom found in bulk (R),[49] the nanoparticle deviation from the bulk reference interatomic distance resulting from the fit (ΔR), the energy shift parameter (E_0), which was fixed for pathways consisting of the same absorbing and scattering atom, and the mean-squared disorder (σ^2). A reasonable estimate of the error associated with the degeneracy and mean-squared disorder values $(N_{exp}$ and $\sigma^2)$ is 10%[29,46,47] and an estimate of error for ΔR and E_0 is 5%.[47] Additional higher-order shell pathway parameters are included in Supporting Information Table S5.

We can use the fcc Ni + substitutional P model to estimate the amount of P in the nanoparticles by examining the degeneracy of the pathways. The P content is determined by summing the degeneracy values (i.e., N_{exp}) for the Ni−P pathways and dividing by the sum of the degeneracies for all pathways (see Supporting Information for methods). This same method is used to determine the number of Ni atoms in ordered and disordered fcc positions. The first three columns of Table 2 show the estimated percentages of each type of

Table 2. Summary of Ni and P Content from EXAFS Modeling and ICP[a]

% atoms Ni fcc, ordered	% atoms Ni fcc, distorted	% atoms P (substitutional)	% atoms P from ICP results
79.2%	15.5%	5.3%	6.4%

[a]The first two columns show the % contribution of the Ni atoms in both ordered and distorted positions with respect to the fcc Ni lattice. In the third column is the phosphorus atomic percentage calculated from EXAFS modeling. The P is located on substitutional fcc sites. The final column lists the average phosphorus content determined from ICP results.

Table 1. First and Second Shell Path Parameters[a]

			ordered Ni−Ni pathways from fcc			
pathway	N_{theory}	N_{exp}	R (Å)	ΔR (Å)	E_0 (eV)	σ^2 (Å^2) × 10^{-3}
Ni−Ni (shell 1)	12	9.49	2.49	−0.003	6.26	7.73
Ni−Ni (shell 2)	6	4.72	3.52	−0.008	6.26	12.0
			Ni−Ni pathways (Ni_3P fcc model)			
pathway	N_{theory}	N_{exp}	R (Å)	ΔR (Å)	E_0 (eV)	σ^2 (Å^2) × 10^{-3}
Ni−Ni (shell 1)	8	1.68	2.49	0.277	6.26	13.8
Ni−Ni (shell 2)	6	1.25	3.52	−0.280	6.26	14.0
			Ni−P pathways (Ni_3P fcc model)			
pathway	N_{theory}	N_{exp}	R (Å)	ΔR (Å)	E_0 (eV)	σ^2 (Å^2) × 10^{-3}
Ni−P (shell 1)	4	0.83	2.49	−0.194	−8.70	8.95
Ni−P (shell 2)	8	1.65	4.32	0.094	−8.70	9.13

[a]Parameters are listed for fcc Ni and for the artificial Ni_3P fcc model used to construct the best-fit EXAFS model for the Ni nanoparticle sample.

contribution (Ni in ordered fcc positions, Ni in distorted fcc positions surrounding the substitutional P atoms, and P from substitution on fcc sites). The estimated P percentage in the structure from the model fit, based on the number of phosphorus atoms in the 5.57 Å radial shell, is 5.3%. This is a large amount of P and an unexpected result considering that XRD only shows the fcc phase and no detectable phosphide compounds. Furthermore, the result is important considering that many groups have used this synthetic method for their Ni nanoparticles, which they assume to be pure fcc Ni. In a similar finding in bulk materials, retention of the Ni fcc lattice has been observed in bulk Ni−P alloys with atomic percentage of P up to 14%.[41] In these bulk Ni−P samples the Ni fcc lattice was maintained with good crystallinity despite the high phosphorus content.[41] This suggests that such phosphorus incorporation on substitutional sites may also be possible at the nanoscale.

To confirm that the P contribution is not from TOP surface ligands, ICP-OES (inductively coupled plasma-optical emission spectrometry) was performed on Ni nanoparticles for Ni, P, and C contents. The atomic percentages in the sample were found to be 83.3, 5.0, and 11.7% for Ni, P, and C, respectively (Table 3). If we consider that all the detected carbon atoms are

Table 3. The Elemental Composition of Ni Nanoparticles Synthesized through Standard Techniques Based on ICP Measurements[a]

element	Ni	P	C
atomic %	83.3	5.0	11.7

[a]From these results, the carbon content is an order of magnitude too small in comparison to the phosphorus atomic % for the phosphorus to be a result of TOP surface ligand contributions.

from TOP, which has 24 C atoms and 1 P atom in its molecule, then the C/P ratio should be 24:1. But the C/P ratio from our ICP is nearly an order of magnitude smaller than what would be expected from the TOP ligand molecules. This confirms that most of the P atoms are contained within the Ni nanoparticles and not located on the surface in the form of TOP molecules.

This high P content is repeatable across multiple syntheses. Results from ICP analysis on eight Ni samples from identical synthesis conditions results in an average of 6.4 atomic % P in the Ni nanoparticles (Table 2, column 4) with a standard deviation of 1.9 atomic % P.

We also calculate the surface coverage by TOP ligands of our Ni nanoparticles. Using the carbon content as a guide we find that only 12% of the surface Ni atoms are connected with TOP molecules. A comparable surface ligand coverage has been previously observed,[50] and nanoparticle phosphine ligand coverage has been shown to decrease with increasing particle size,[51] which is relevant to our larger nanoparticles. The low TOP coverage explains the slow precipitation behavior of the Ni nanoparticles in a nonpolar solvent such as hexane.

As another test to prove that the P contribution is not from surface TOP surfactant, a ligand exchange was performed on the Ni nanoparticles, exchanging the existing ligands for oleic acid (see Supporting Information for methods). ICP analysis was then performed on both the as-prepared (with TOP surfactant) nanoparticles and the nanoparticles after ligand exchange. Results of P content between the two samples showed negligible changes (5.0 atomic % P before ligand exchange versus 5.2 atomic % P after ligand exchange) confirming that the P content measured by ICP is not dominated by surface phosphine.

To further investigate the synthetic conditions for P inclusion, the effects of reaction temperature and time on the P content of the Ni nanoparticles were studied. Plotting P content for reactions at 210, 220, and 230 °C, with samples taken at 20, 40, and 60 min, shows a consistent increase in P content within the nanoparticles as a function of reaction temperature and time (Figure 4a). This result further confirms that the P content is incorporated into the nanocrystal and not merely on the surface. Additionally, the wide variance of P content in the 230 °C samples (open red symbols in Figure 4a) demonstrates that P incorporation at higher reaction temperatures is sensitive to minor changes in synthetic conditions. TEM images of the nanoparticles synthesized with varied conditions are included in the Supporting Information (Figure S5).

A trend of lattice expansion due to the P doping is clearly shown in Figure 4b. The (111) 2-θ peak from reference (JCPDS 65-2865) is 44.5°. The P doped nanoparticle samples show XRD peaks shifted toward lower angles. The black line in Figure 4b is linearly fitted with the results from P doped Ni nanoparticles and the Ni reference ($Y = -0.0535X + 44.522$, $R^2 = 0.7445$). From this equation, it is possible to roughly predict the P content of Ni nanoparticles from an XRD pattern. The d-spacing is also calculated based on the peak position (Figure
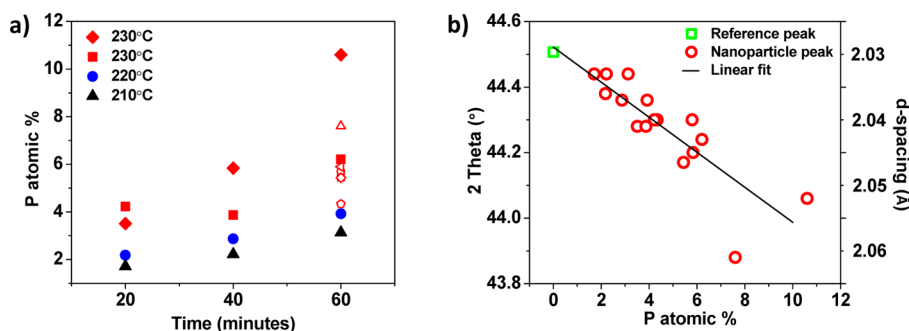

Figure 4. Implications of synthetic parameters on Ni nanoparticle P atomic % and corresponding XRD peak shifts. (a) Correlations between reaction temperature and time. The black, blue, and red solid symbols represent the P atomic % of samples synthesized at 210, 220, and 230 °C, respectively, for different reaction times. All of the open symbols exhibit P atomic % from the samples synthesized at 230 °C for 60 min. (b) The correlation between the P atomic % and the (111) peak position of Ni nanoparticle samples and the Ni reference. The green open square represents the (111) 2-θ peak position (44.5°) of Ni reference (JCPDS 65-2865). The red open circles represent the (111) 2-θ peak positions of the samples which show P contents. The d-spacing of (111) plane is also calculated based on the peak positions, showing the lattice expansion due to P doping.

4b). At a P content of ~10 atomic %, there is a ~1% expanded lattice constant.

Figure 3 shows the deviations in atomic position as a percentage of the reference crystalline atomic positions (ΔR%) for the first and second shell atoms. The atoms are categorized by the following structural contributions: (1) Ni−Ni from fcc Ni, (2) Ni−P from substitutional P on fcc sites, and (3) Ni−Ni from Ni on fcc sites which are allowed to distort, representing the Ni atoms which surround the substitutional P. For our Ni nanoparticle samples the majority (79.2%) of the fcc Ni pathways deviate minimally from the bulk interatomic distances, with $\Delta R/R < 0.25\%$. These deviations are similar in magnitude to the Ni foil deviations (compare red bars in Figure 3, Ni foil versus Ni nanoparticles). This means that the majority of Ni atoms are located on the fcc lattice. As a result, the bulk-like fcc Ni contributions within the Ni nanoparticle sample are detectable by XRD. A smaller portion of the Ni−Ni pathways within the nanoparticles (blue bars in Figure 3), have large ΔR values, representing Ni atoms that deviate from their fcc positions, likely as a result of nearby substitutional P. These Ni−Ni contributions are described by the fcc Ni_3P component of the model. The Ni−P pathways resulting from P substitution on the fcc lattice (green bars in Figure 3) also show deviations from ideal fcc positions, yet they are smaller than the deviations of the distorted Ni−Ni pathways. The P atoms may not be sitting in ideal fcc sites because (1) a small number of the P atoms may be positioned in octahedral sites, as suggested by our Ni/Ni_2P EXAFS model (see Supporting Information), (2) the P atoms may be positioned slightly off the fcc lattice sites, or (3) the P atoms may take the form of dimers within the structure, as suggested by our density-functional calculations (vide infra). All aforementioned phenomena would cause the interatomic distances to deviate slightly from the value of the ideal fcc Ni phase. The possibility of the P atoms sitting in grain boundaries within the nanoparticles was considered. This is unlikely because the grain boundaries effectively act as a surface at which the degeneracy values of higher order shells is known to be significantly diminished due to the surface termination effect[43,45] and we do not observe this effect in our EXAFS model. Comparing the average mean-squared disorder values (Table 1, Supporting Information Figure S6), we see that the disorder is larger for the nanoparticles than for bulk (foil), meaning that the nanoparticle pathways have a higher degree of structural disorder. In addition, the distorted Ni−Ni pathways show larger values than the ordered Ni−Ni pathways, revealing that these pathways not only show greater distance deviation, but also are distributed in a less-uniform manner.

The unusually high P content in the Ni nanoparticles (6.4 atomic % by ICP (average), 5.3 atomic % by EXAFS) raises the question about the oxidation state of the P and the feasibility of P substitution at such high concentrations with relative retention of the structural integrity of the fcc lattice. DFT calculations including spin-polarization (see Supporting Information for computational details) of the charge density and Bader analysis[52] for an fcc Ni supercell containing a single substituted P atom ($Ni_{107}P$) show only a small amount of charge transfer of less than $0.25e$ between the P and the Ni atoms. A small Bader charge transfer of 0.25 electrons between P and Ni indicates that the bonding is mostly covalent in nature with some ionic character, which is consistent with the electronegativity values of P and Ni (see Supporting Information). This suggests that the P has an oxidation state of zero within the fcc Ni phase. This is confirmed by our XAS

results, which reveal little deviation from fcc Ni in the near edge region (XANES), showing that the Ni atoms (and therefore P atoms, due to charge-neutrality) have an oxidation number of zero.

The positions of the P atoms in the Ni lattice were also compared between the relaxed structures from the DFT calculations and our EXAFS models. Through EXAFS modeling, it was found that P atoms sit primarily on substitutional sites. DFT defect formation energies were calculated to determine the energetics of various possible positions of phosphorus atoms in fcc Ni. The formation energy for a P atom to sit substitutionally on an fcc lattice site is 0.8 eV (see Table 4). The formation energy for the interstitial sites is

Table 4. Formation Energy Calculation Results[a]

TM	supercell	E_f (eV)
Ni	$Ni_{108}P$ (o)	2.7
	$Ni_{108}P$ (t)	3.9
	$Ni_{107}P$ (s)	0.8
Co	$Co_{96}P$ (o)	3.3
	$Co_{96}P$ (t)	3.5
	$Co_{95}P$ (s)	0.7
Fe	$Fe_{128}P$ (o)	3.4
	$Fe_{128}P$ (t)	3.4
	$Fe_{127}P$ (s)	0.4

[a]Calculated formation energies for octahedral (o), tetrahedral (t), and substitutional (s) P for Ni, Co, and Fe.

higher. It is 2.7 eV for the octahedral site and 3.9 eV for the tetrahedral site. On the basis of the formation energies, it is not surprising that the majority of the P atoms are found by the EXAFS analysis in both the fcc Ni + Ni_2P and the fcc Ni + substitutional P models, to be located on substitutional sites. However, the results of the fcc Ni + Ni_2P EXAFS modeling suggesting that ~17% of the Ni−P pathways correspond to octahedral position radial distances is somewhat unexpected. Together, the EXAFS analysis and the DFT defect formation energies show that the majority of the P atoms are positioned on fcc lattice sites.

The analysis of the P location in Ni was extended to several other important transition metal (TM) systems. Table 4 shows the formation energies for the P-doped ferromagnetic transition metals (TMs, TM = Ni, Co, Fe), where P is present at tetrahedral or octahedral interstitial lattice positions or substituted for a TM atom. Total energies were calculated using (spin-polarized) DFT. Formation energies, E_f, were calculated as $E_f = [E[TM_nP_m] - (n\mu_{TM} + m\mu_P)]/m$, where $E[TM_nP_m]$ denotes the total energy of the cell containing n TM atoms and m P atoms, and μ_{TM} and μ_P denote the chemical potentials of TM and P, respectively. μ_{TM} was taken as the total energy per atom of TM in the appropriate crystal structure (i.e., fcc, hcp, bcc, for TM = Ni, Co and Fe, respectively), and μ_P was calculated as $\mu_P = (E[TM_3P] - (24 \mu_{TM}))/8$, where $E[TM_3P]$ is the total energy of the TM_3P phase, calculated for a unit cell containing 24 TM ions and 8 P ions. Even when considering that the diffusion of a P atom as a substitutional impurity into a transition metal nanoparticle will require the formation of a vacancy and comparing the combined formation energy of a TM vacancy and a P atom substituted for a TM atom, substitutional rather than interstitial doping is significantly favored in all three TMs. Similarly, ε-phase Co has been found
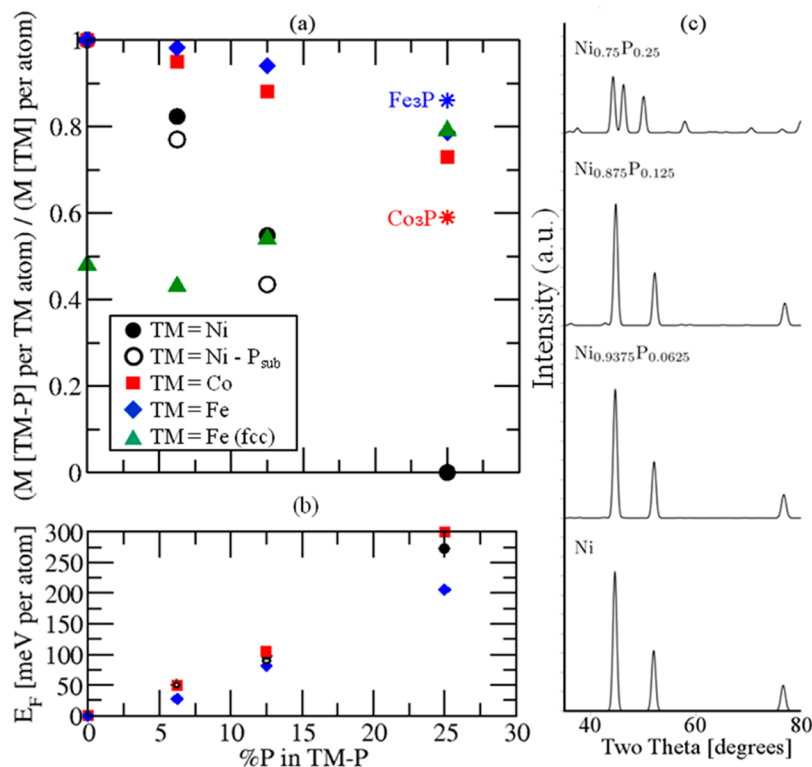
Figure 5. DFT calculations for phosphorus doping in transition metals (TMs): magnetization, formation energies, and diffraction patterns. (a) Magnetization M per TM atom for the TMs Ni (filled black circles), Co (red squares), and Fe (blue diamonds), substitutionally doped with P. The green triangles give the magnetization for P-doped fcc Fe. Magnetizations for the Co_3P and Fe_3P crystal structures are indicated by the red and blue stars, respectively. Empty black circles give the magnetization for Ni containing substitutional P dimers. (b) Formation energies E_f for P-doped Ni (filled black circles), Co (red squares), and Fe (blue diamonds). Empty black circles give the formation energy for Ni containing substitutional P dimers. Formation of P dimers in Ni was found to be energetically slightly favorable with respect to evenly distributed P. (c) Calculated XRD patterns for pure and P-doped Ni.

experimentally to favor substitutional rather than interstitial P-doping.[48]

Figure 5b shows the formation energies calculated for P-doped TM at concentrations of 6.25, 12.5, and 25 atomic %. At 6.25 atomic % P, the formation energies for the P-doped TMs are small (within 60 meV per atom), suggesting that P may be accommodated within the TM lattice at this concentration. As the concentration of P increases, the formation energy of the doped TM also increases, indicating that substitutional doping becomes less favorable. At 12.5 atomic % P, the formation energy is still less than ~100 meV per atom, which is consistent with the observation of fcc Ni doped at 14 atomic % P.[41] Formation of P dimers (empty black circles) in Ni was found to be energetically slightly favorable with respect to evenly distributed P (filled black circles), for concentrations of 6.25 and 12.5 atomic % P, supporting the hypothesis of P-clustering.

Experimentally, Ni has been found to accommodate up to 14 atomic % P without departing significantly from the fcc crystal structure.[41] Calculated XRD patterns for the relaxed Ni–P cells (Figure 5c) are consistent with this result, indicating that the fcc structure is retained at P concentrations of 6.25 and 12.5 atomic % for which the XRD patterns are almost indistinguishable from that of pure Ni. At 25 atomic % P, the relaxed cell is deformed significantly with respect to the fcc structure, as is reflected in the altered XRD pattern. The Ni–P compound with the lowest phosphorus concentration in bulk materials is Ni_3P, which has 25 atomic % P and exhibits a tetragonal structure.[53]

Surprisingly, in contrast to our experimental results, the calculated lattice constant and bulk modulus for P-doped Ni, for concentrations of 6.25 and 12.5 atomic % P indicate that the lattice undergoes a contraction as the concentration of P is increased, consistent with the smaller covalent radius of P compared to Ni. The bulk modulus is increased by ~1% for Ni doped at 12.5 atomic % P compared to pure Ni (see Supporting Information Table S6). Because the experimental results show a lattice expansion rather than contraction, this implies that some of the P formation may occur on octahedral interstitial sites, instead of solely fcc substitutional sites. This finding is consistent with the EXAFS positions analyzed using the fcc Ni + Ni_2P model.

Phosphorus doping is expected to reduce the magnetism of Ni nanoparticles. Figure 5a shows the calculated magnetization M against the concentration of substitutional P, for fcc Ni (filled black circles). P is substituted for Ni and the atomic positions and cell size and shape are relaxed until the forces on all ions are less than 0.03 eV/Å. The calculations were carried out with periodic boundary conditions using supercells containing a single P atom, for P concentrations of 6.25, 12.5, and 25 atomic %. The magnetization decreases for the P-doped Ni with increasing P doping. The decrease in magnetization with P concentration is considerable, falling to zero by 25 atomic % P, exhibiting paramagnetism in Ni_3P.[54]

Through our DFT calculations we can estimate the P effect on magnetization to be expected in our nanoparticles. For Ni doped with 6.25 atomic % P, which is close to the concentration measured to be present in the nanoparticles

described in this article, M is calculated as 0.49 μ_B per Ni atom, which is equivalent to 45 emu/g, compared to the value obtained using a SQUID of ~29.5 emu/g (see Figure 6). This
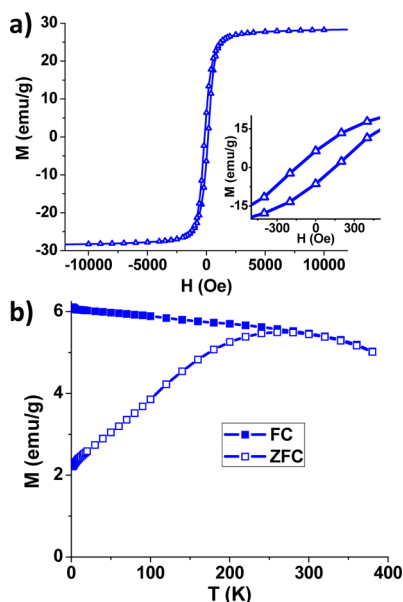

Figure 6. Magnetization data for Ni nanoparticles. (a) Magnetization versus applied field hysteresis loops measured at 2 K. (b) FC and ZFC magnetization curves for Ni nanoparticles. The curves represent temperature dependence of the magnetization for samples under a magnetic field of 100 Oe after zero-field cooling (open square) and field cooling (filled square).

discrepancy might be explained by P clustering. The empty black circles in Figure 5a give the magnetization for P dimers within the Ni lattice. The dimers lead to slightly lower magnetizations than the evenly distributed P for the same concentration. For the dimers, P was substituted for two adjacent Ni atoms in a supercell that is twice as large as that used for the calculations corresponding to the evenly distributed P (i.e., the filled black circles). The lower magnetization of the Ni doped with P dimers indicates that clusters of P within the Ni lattice would disrupt the ferromagnetism more than evenly distributed P; P clustering might therefore be expected to lead to a greater reduction in M, leading to closer agreement with the measured saturation moment.

The loss of magnetization due to P content is also supported by our experimental data. Magnetization versus applied-field (M vs H) hysteresis loops for the Ni nanoparticle sample at 2 K are shown in Figure 6a. The Ni nanoparticles show lower remnant magnetization (M_r) (6.4 emu/g) and saturation magnetization (M_s) (29.5 emu/g) than those observed in bigger Ni nanoparticles reported previously.[55,56] This decrease, although likely due in part to the size of domains in our Ni nanoparticles, which are smaller than the critical size for superparamagnetism,[55,57,58] may also be a function of phosphorus content within the nanoparticle structure, as suggested by our theoretical calculations. Zero-field cooling (ZFC)−field cooling (FC) measurements also display significant changes in magnetic properties (Figure 6b). The blocking temperature (T_b) of the Ni nanoparticles is around 260 K, which is lower than that observed in the bulk structure.

Two additional samples were synthesized to investigate the effects of phosphorus on the magnetic properties: (1) Ni nanoparticles synthesized without TOP and (2) Ni nanoparticles synthesized with half the amount of TOP (2.24 mmol) compared to the standard Ni nanoparticle synthesis TOP concentration (4.48 mmol). Compared to the "standard" Ni synthesis, nanoparticles synthesized with less TOP are larger and irregular in morphology (size, 32.8 nm; std. dev, 14.4%) (Supporting Information Figure S7, left). Nanoparticles synthesized without TOP (Supporting Information Figure S7, right) exhibit an even greater polydispersity and a larger average size compared to the "standard" Ni nanoparticles (size, 32.3 nm; std. dev, 27.8%). The samples synthesized with less TOP and without TOP do not clearly show the T_b point within our measurement temperature range (2−380 K) indicating that these samples exhibit more bulk-like (higher blocking temperature) magnetic behavior (Supporting Information Figure S8).[59] Additionally, field dependence of the magnetization results of the samples with lower TOP concentrations show a larger hysteresis loop with higher M_r (Ni without TOP, 15.9 emu/g; Ni with less TOP, 10.34 emu/g) and M_s (Ni without TOP, 34.5 emu/g; Ni with less TOP, 36.2 emu/g) than that of standard Ni nanoparticles. However it is not clear whether or not this effect is solely a result of phosphorus content, since ferromagnetic behavior is highly sensitive to size effects.[60−62] This change in magnetic behavior with increasing phosphorus content suggests that changes in the nanoparticle properties may result from the presence of excess phosphorus within the structure.

DFT calculations were carried out to investigate whether the P doping effects on magnetization may be applicable to other transition metal systems. Figure 5a shows the calculated magnetization against substitutional P concentration for hexagonal close-packed (hcp) Co (red squares) and body-centered cubic (bcc) Fe (blue diamonds). As with Ni, the magnetization decreases for Co and Fe with increasing P doping, although there is a weaker sensitivity of the ferromagnetism in these TMs to P doping compared to Ni. This effect is consistent with the fact that the TM$_3$P phase exhibits ferromagnetism rather than paramagnetism in Co$_3$P[63] and Fe$_3$P.[64]

In addition, the catalytic properties of the Ni nanoparticles may be severely affected by the unintended P doping. The density of states (DOS) near the Fermi surface affects how a molecule can bind to the material, as the molecular orbitals form bonding and antibonding states with the surface states. According to our DOS calculations, the majority states at 100 meV above the Fermi level are strongly affected by the P presence, which reduces the number of states. Comparing doped (6.25 atomic % P) Ni to pure Ni, there is a 40% reduction in the number of states observed at 100 meV (Figure 7). This is particularly significant because these nanoparticles are notable for their use in catalytic applications, and properties of catalytic materials are very sensitive to surface states, therefore the excess P content may detrimentally degrade the catalytic properties of these Ni nanoparticles.

Through a combination of characterization techniques, including EXAFS to probe short-range structural order and XRD to determine the long-range crystal structure, as well as DFT, TEM, SQUID, and XANES, we were able to elucidate the structure of Ni nanoparticles and derive conclusions concerning the relation of their synthetic conditions to the resulting structure−property relations. Using TOP to promote
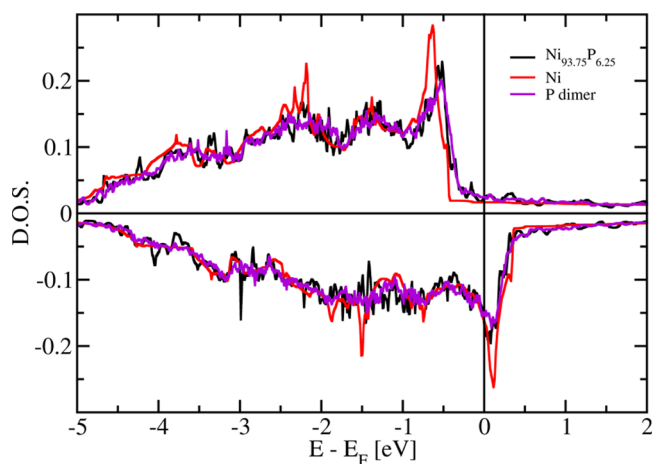
Figure 7. Bulk Ni DOS near the Fermi surface. The majority states around 100 meV above the Fermi level are strongly affected by the P content. Substitutional P (6.25 atomic %) is shown for evenly distributed P (black) and for P dimers (purple). The P presence reduces the number of states in both cases.

stabilization and coordination in Ni nanoparticle synthesis can also lead to undesired phosphorus doping. This phosphorus doping increases as a function of synthetic temperature and reaction time. This is likely relevant to other synthetic systems which employ TOP and similarly strong-binding phosphorus ligands, such as triphenyl phosphine. Even with phosphorus content as high as several percent, the crystalline fcc Ni lattice is not significantly disrupted. There is, however, a lattice expansion notable in the XRD pattern as a function of P atomic %, which enables calculation of the P content of the nanoparticles based on XRD peak position alone, a useful technique in fine-tuning the synthesis. We find that the structure consists of a crystalline fcc lattice with P substitutional atoms and distortion only of the Ni atoms surrounding the P substitutional sites. This unintentional P doping significantly impacts the nanoparticle structural behavior, magnetic properties, and catalytic activities, which we have demonstrated through both the experimental and modeled phenomena.

The results of this study suggest that it should be taken into consideration in optimizing nanoparticles for use in applications, that there may be a significant concentration of XRD amorphous species present in the nanoparticles, which may interfere with desired properties. Thus care should be taken when using strong binding surfactant ligands such as TOP in the synthesis of nanoparticles, particularly when they are used in high concentrations.

ASSOCIATED CONTENT

Ⓢ Supporting Information
Detailed experimental section, Figures S1–S8, and Tables S1–S6. This material is available free of charge via the Internet at http://pubs.acs.org.

AUTHOR INFORMATION

Corresponding Author
*E-mail: rdr82@cornell.edu.

Author Contributions
[†]Authors contributed equally to this work

Notes
The authors declare no competing financial interest.

ACKNOWLEDGMENTS

REFERENCES

(1) Murray, C. B.; Norris, D. J.; Bawendi, M. G. *J. Am. Chem. Soc.* **1993**, *115*, 8706−8715.
(2) Yin, Y.; Alivisatos, A. P. *Nature* **2005**, *437*, 664−670.
(3) Murray, C. B.; Kagan, C. R.; Bawendi, M. G. *Annu. Rev. Mater. Sci.* **2000**, *30*, 545−610.
(4) Peng, X.; Manna, U.; Yang, W.; Wickham, J.; Scher, E.; Kadavanich, A.; Allvisatos, A. P. *Nature* **2000**, *404*, 59−61.
(5) Bealing, C. R.; Baumgardner, W. J.; Choi, J. J.; Hanrath, T.; Hennig, R. G. *ACS Nano* **2012**, *6*, 2118−2127.
(6) Liu, H.; Owen, J. S.; Alivisatos, A. P. *J. Am. Chem. Soc.* **2007**, *129*, 305−312.
(7) Wang, F.; Tang, R.; Buhro, W. E. *Nano Lett.* **2008**, *8*, 3521−3524.
(8) Evans, C. M.; Evans, M. E.; Krauss, T. D. *J. Am. Chem. Soc.* **2010**, *132*, 10973−10975.
(9) Owen, J. S.; Park, J.; Trudeau, P.-E.; Alivisatos, A. P. *J. Am. Chem. Soc.* **2008**, *130*, 12279−12281.
(10) Zhang, H.; Ha, D.-H.; Hovden, R.; Kourkoutis, L. F.; Robinson, R. D. *Nano Lett.* **2011**, *11*, 188−197.
(11) Hanada, N.; Ichikawa, T.; Fujii, H. *J. Phys. Chem. B* **2005**, *109*, 7188−7194.
(12) Wu, S.-H.; Chen, D.-H. *J. Colloid Interface Sci.* **2003**, *259*, 282−286.
(13) Ozay, O.; Aktas, N.; Inger, E.; Sahiner, N. *Int. J. Hydrogen Energy* **2011**, *36*, 1998−2006.
(14) Mahata, N.; Cunha, A. F.; Orfao, J. J. M.; Figueiredo, J. L. *Appl. Catal.* **2008**, *351*, 204−209.
(15) Lin, K. Y.; Tsai, W. T.; Chang, J. K. *Int. J. Hydrogen Energy* **2010**, *35*, 7555−7562.
(16) Lin, K. Y.; Tsai, W. T.; Yang, T. J. *J. Power Sources* **2011**, *196*, 3389−3394.
(17) Yang, C. C.; Li, Y. J.; Chen, W. H. *Int. J. Hydrogen Energy* **2010**, *35*, 2336−2343.
(18) Kim, C.; Noh, M.; Choi, M.; Cho, J.; Park, B. *Chem. Mater.* **2005**, *17*, 3297−3301.
(19) Park, J.; Kang, E.; Son, S. U.; Park, H. M.; Lee, M. K.; Kim, J.; Kim, K. W.; Noh, H.-J.; Park, J.-H.; Bae, C. J.; Park, J.-G.; Hyeon, T. *Adv. Mater.* **2005**, *17*, 429−434.
(20) Park, J.; Joo, J.; Kwon, S. G.; Jang, Y.; Hyeon, T. *Angew. Chem., Int. Ed.* **2007**, *46*, 4630−4660.
(21) Muthuswamy, E.; Savithra, G. H. L.; Brock, S. L. *ACS Nano* **2011**, *5*, 2402−2411.
(22) Henkes, A. E.; Vasquez, Y.; Schaak, R. E. *J. Am. Chem. Soc.* **2007**, *129*, 1896−1897.
(23) Wang, J.; Johnston-Peck, A. C.; Tracy, J. B. *Chem. Mater.* **2009**, *21*, 4462−4467.
(24) Chiang, R.-K.; Chiang, R.-T. *Inorg. Chem.* **2007**, *46*, 369−371.

(25) Gao, J.; Guan, F.; Zhao, Y.; Yang, W.; Ma, Y.; Lu, X.; Hou, J.; Kang, J. *Mater. Chem. Phys.* **2001**, *71*, 215−219.

(26) Peng, T. C.; Xiao, X. H.; Wu, W.; Fan, L. X.; Zhou, X. D.; Ren, F.; Jiang, C. Z. *J. Mater. Sci.* **2012**, *47*, 508−513.

(27) Carenco, S.; Boissiere, C.; Nicole, L.; Sanchez, C.; Le, F. P.; Mezailles, N. *Chem. Mater.* **2010**, *22*, 1340−1349.

(28) Aruguete, D. M.; Marcus, M. A.; Li, L. S.; Williamson, A.; Fakra, S.; Gygi, F.; Galli, G. A.; Alivisatos, A. P. *J. Phys. Chem. C* **2007**, *111*, 75−79.

(29) Marcus, M. A.; Flood, W.; Stiegerwald, M.; Brus, L.; Bawendi, M. *J. Phys. Chem.* **1991**, *95*, 1572−1576.

(30) Cheng, G.; Carter, J. D.; Guo, T. *Chem. Phys. Lett.* **2004**, *400*, 122−127.

(31) Park, J.-I.; Kim, M. G.; Jun, Y.-W.; Lee, J. S.; Lee, W.-R.; Cheon, J. *J. Am. Chem. Soc.* **2004**, *126*, 9072−9078.

(32) Sarma, L. S.; Chen, C.-H.; Kumar, S. M. S.; Wang, G.-R.; Yen, S.-C.; Liu, D.-G.; Sheu, H.-S.; Yu, K.-L.; Tang, M.-T.; Lee, J.-F.; Bock, C.; Chen, K.-H.; Hwang, B.-J. *Langmuir* **2007**, *23*, 5802−5809.

(33) Rodriguez, J. A.; Hanson, J. C.; Kim, J.-Y.; Liu, G.; Iglesias-Juez, A.; Fernandez-Garcia, M. *J. Phys. Chem. B* **2003**, *107*, 3535−3543.

(34) Rockenberger, J.; Troeger, L.; Kornowski, A.; Vossmeyer, T.; Eychmueller, A.; Feldhaus, J.; Weller, H. *J. Phys. Chem. B* **1997**, *101*, 2691−2701.

(35) Frenkel, A. I.; Hills, C. W.; Nuzzo, R. G. *J. Phys. Chem. B* **2001**, *105*, 12689−12703.

(36) Bunker, G. *Introduction to XAFS: a practical guide to X-ray absorption fine structure spectroscopy*; Cambridge University Press: Cambridge, 2010; p 260.

(37) Stern, E. A. *Phys. Rev. B* **1974**, *10*, 3027−3037.

(38) Stern, E. A. *Contemp. Phys.* **1978**, *19*, 289−310.

(39) Mantina, M.; Wang, Y.; Chen, L. Q.; Liu, Z. K.; Wolverton, C. *Acta Mater.* **2009**, *57*, 4102−4108.

(40) Chan, T. L.; Tiago, M. L.; Kaxiras, E.; Chelikowsky, J. R. *Nano Lett.* **2007**, *8*, 596−600.

(41) Song, J.; Wei, Z.; Pan, Z.; Xie, Z.; Wei, S. *AIP Conf. Proc.* **2007**, *882*, 453−456.

(42) Blanchard, P. E. R.; Grosvenor, A. P.; Cavell, R. G.; Mar, A. *J. Mater. Chem.* **2009**, *19*, 6015−6022.

(43) Anspoks, A.; Kuzmin, A. *J. Non-Cryst. Solids* **2011**, *357*, 2604−2610.

(44) Arcon, I.; Tuel, A.; Kodre, A.; Martin, G.; Barbier, A. *J. Synchrotron Radiat.* **2001**, *8*, 575−577.

(45) Calvin, S.; Miller, M. M.; Goswami, R.; Cheng, S. F.; Mulvaney, S. P.; Whitman, L. J.; Harris, V. G. *J. Appl. Phys.* **2003**, *94*, 778−783.

(46) Gurman, S. J. *J. Synchrotron Radiat.* **1995**, *2*, 56−63.

(47) Nietubyc, R.; Czerwosz, E.; Diduszko, R.; Dluzewski, P.; Kozlowski, M.; Welter, E. *J. Alloys Compd.* **2009**, *484*, 896−901.

(48) Ha, D.-H.; Moreau, L. M.; Bealing, C. R.; Zhang, H.; Hennig, R. G.; Robinson, R. D. *J. Mater. Chem.* **2011**, *21*, 11498−11510.

(49) Häglund, J.; Fernández Guillermet, A.; Grimvall, G.; Körling, M. *Phys. Rev. B* **1993**, *48*, 11685.

(50) Moreels, I.; Justo, Y.; De, G. B.; Haustraete, K.; Martins, J. C.; Hens, Z. *ACS Nano* **2011**, *5*, 2004−2012.

(51) Katari, J. E. B.; Colvin, V. L.; Alivisatos, A. P. *J. Phys. Chem.* **1994**, *98*, 4109−4117.

(52) Bader, R. *Atoms in Molecules: A Quantum Theory*; Oxford University Press: New York, 1994.

(53) Oryshchyn, S.; Babizhetskyy, V.; Chykhriy, S.; Aksel'rud, L.; Stoyko, S.; Bauer, J.; Guerin, R.; Kuz'ma, Y. *Inorg. Mater.* **2004**, *40*, 380−385.

(54) Konig, E. Ni(0), Ni(I). In *SpringerMaterials- The Landolt-Bornstein Database*, Hellwege, K.-H.; Hellwege, A. M. (accessed September 30, 2011).

(55) Gong, W.; Li, H.; Zhao, Z.; Chen, J. *J. Appl. Phys.* **1991**, *69*, 5119−5121.

(56) Zhang, H. T.; Wu, G.; Chen, X. H.; Qiu, X. G. *Mater. Res. Bull.* **2006**, *41*, 495−501.

(57) Leslie-Pelecky, D. L.; Rieke, R. D. *Chem. Mater.* **1996**, *8*, 1770−1783.

(58) Du, Y.; Xu, M.; Wu, J.; Shi, Y.; Lu, H.; Xue, R. *J. Appl. Phys.* **1991**, *70*, 5903−5905.

(59) Jun, Y.-w.; Seo, J.-w.; Cheon, J. *Acc. Chem. Res.* **2008**, *41*, 179−189.

(60) Johnson, D.; Perera, P.; O'Shea, M. J. *J. Appl. Phys.* **1996**, *79*, 5299−5301.

(61) Roy, S.; Dubenko, I.; Edorh, D. D.; Ali, N. *J. Appl. Phys.* **2004**, *96*, 1202−1208.

(62) Blanco-Mantecon, M.; O'Grady, K. *J. Magn. Magn. Mater.* **2006**, *296*, 124−133.

(63) Konig, E.; Konig, G. Co(0), Co(I). In *SpringerMaterials- The Landolt-Bornstein Database*, Hellwege, K.-H.; Hellwege, A. M. (accessed September 30, 2011).

(64) Konig, E.; Konig, G. Part 2. In *SpringerMaterials- The Landolt-Bornstein Database*, Hellwege, K.-H.; Hellwege, A. M. (accessed September 30, 2011).